

On the Prospects for Detection and Identification of Low-Frequency Oscillation Modes in Rotating B Type Stars

J. Daszyńska-Daszkiewicz¹, W.A. Dziembowski^{2,3}
and A.A. Pamyatnykh^{3,4}

¹Instytut Astronomiczny, Uniwersytet Wrocławski. ul. Kopernika 11, Poland
e-mail: daszynska@astro.uni.wroc.pl

²Warsaw University Observatory, Al. Ujazdowskie 4, 00-478 Warsaw, Poland
e-mail: wd@astrouw.edu.pl

³Copernicus Astronomical Center, ul. Bartycka 18, 00-716 Warsaw, Poland
e-mail: alosza@camk.edu.pl

⁴Institute of Astronomy, Pyatnitskaya Str. 48, 109017 Moscow, Russia

ABSTRACT

We study how rotation affects observable amplitudes of high-order g- and mixed r/g-modes and examine prospects for their detection and identification. Our formalism, which is described in some detail, relies on a nonadiabatic generalization of the traditional approximation. Numerical results are presented for a number of unstable modes in a model of SPB star, at rotation rates up to 250 km/s. It is shown that rotation has a large effect on mode visibility in light and in mean radial velocity variations. In most cases, fast rotation impairs mode detectability of g-modes in light variation, as Townsend (2003b) has already noted, but it helps detection in radial velocity variation. The mixed modes, which exist only at sufficiently fast rotation, are also more easily seen in radial velocity. The amplitude ratios and phase differences are strongly dependent on the aspect, the rotational velocity and on the mode. The latter dependence is essential for mode identification.

Stars: oscillations – Stars: emission-line, Be – Stars: rotation

1 Introduction

Variability with frequencies comparable to rotation frequency has been found in a number of hot (most often Be) stars. Whether such variability is caused by slow modes has been debated for some time (see *e.g.*, Baade 1982, Balona 1985). However, recent data from the MOST on ζ Oph (Walker *et al.* 2005a), HD 163868 (Walker *et al.* 2005b), and β CMi (Saio *et al.* 2007) revealed rich frequency spectra which may be understood only in terms of oscillation mode excitation. There are also frequency spectra obtained from ground-based observations, such as of μ Eri (Jerzykiewicz *et al.* 2005), which certainly cannot be explained in terms of a rotational modulation. A potential for using the abundant frequency data as constraints on stellar models exists but the prerequisite is mode identification and it has not been done so far.

Most frequently used method of mode identification employs the data on mode amplitudes and phases of light variability in various bands and in radial velocity. Amplitude ratios depend on angular dependence of surface distortion, which in rotating stars is no longer described by a single spherical harmonic. The departure becomes large once the angular velocity of rotation is comparable to oscillation frequency. This is not an unusual situation for cooler B stars in the main sequence band. Take a model of $6 M_{\odot}$ star in the mid of its main sequence evolution. Ignoring effects of rotation, we

find that all dipole modes with period between 1.8 d to 2.8 d are unstable. Rotation periods in this range correspond to equatorial velocities between 100 km/s and 150 km/s, which is not high for such a star.

For low frequency modes the surface dependence may be approximately described in terms of the Hough functions (see *e.g.*, Lee and Saio 1997, Bildsten *et al.* 1996, Townsend 2003a). This approximation, called traditional, was used by Townsend (2003b), who calculated observable light amplitudes and used the results to address the problem of mode identification for low frequencies in rotating stars using multicolor data. It is our experience (*e.g.*, Daszyńska-Daszkiewicz, Dziembowski and Pamyatnykh 2005), however, that in the case of B-type pulsators, it is very important to combine photometric and radial velocity data for a unique discrimination of excited modes and constraining stellar parameters. Thus, this work, which may be regarded as an extension of Townsend's paper, focuses on calculation of radial velocity amplitudes. We adopt an uniform approach in our calculation of all disk-averaged amplitudes and it is different from that used by him. Furthermore, in addition to g-modes, we include r-modes, which become propagative in stellar radiative envelopes once rotation is fast enough (see Savonije 2005, Townsend 2005b, who uses the term mixed gravity-Rossby modes, Lee 2006).

In Section 2, after specifying assumptions adopted in our calculations, we summarize formulae for angular dependence of velocity and atmospheric parameters. Expressions for the light and disk-averaged radial velocity variations are given in Sections 3 and 4, respectively. Sections 5, 6 and 7 present numerical results for selected modes in one representative stellar model considering range of rotation rates but ignoring effects of changes of centrifugal force on model structure. Unstable mode properties are briefly described in Section 5. In Section 6, upon adopting an arbitrary normalization of linear eigenfunctions, we calculate observable amplitudes of various modes, which may be excited and detected. Prospects of mode identification are discussed in Section 7. Examples of diagnostic diagrams employing amplitude ratios and phase differences are shown there.

2 Photospheric Parameter Variations and Velocity Field in the Traditional Approximation

In our study we adopt the standard approximations, which are the linear nonadiabatic theory of stellar oscillation and static plane-parallel atmosphere models. These approximations are well justified in our application. Modes detected in slowly pulsating B-type stars have indeed very low amplitudes, the oscillation periods are much longer than the thermal time scale in the atmosphere, and vertical variations of mode amplitude are small across the whole atmosphere. The constant kinematic acceleration is easily included. Like Townsend (2003b) we adopt the traditional approximation, which allows to separate latitudinal and radial dependencies of the pulsational amplitudes. We essentially follow his formalism, expect that we choose the azimuthal and temporal dependence as $Z = \exp[i(m\varphi - \omega t)]$, which implies $m > 0$ for prograde modes and $m < 0$ for retrograde modes.

The displacement vector at the surface may be written as follows

$$\xi(R, \theta, \varphi) = \varepsilon R \left(\Theta, \frac{\overline{\omega}\hat{\Theta}}{\sin\theta}, -i\frac{\overline{\omega}\tilde{\Theta}}{\sin\theta} \right) Z \quad (1)$$

where ε is an arbitrary, but small, complex constant, and

$$\overline{\omega} = \frac{GM}{\omega^2 R^3}.$$

The three functions Θ , $\hat{\Theta}$, $\tilde{\Theta}$ describe the latitudinal dependence of solutions and are the Hough functions, which are obtained as solutions of the Laplace's tidal equations

$$(\mathcal{D} + ms\mu)\Theta = (s^2\mu^2 - 1)\hat{\Theta}, \quad (2a)$$

$$(\mathcal{D} - ms\mu)\hat{\Theta} = [\lambda(1 - \mu^2) - m^2]\Theta, \quad (2b)$$

where $s = 2\Omega/\omega$ is called the spin parameter, $\mu = \cos\theta$ and $\mathcal{D} \equiv (1 - \mu^2)\frac{d}{d\mu}$. The equations together with boundary conditions at $\mu = 0$ and $\mu = 1$ define the eigenvalue problem on λ . The third function is given by

$$\tilde{\Theta} = -m\Theta + s\mu\hat{\Theta}. \quad (3)$$

Bildsten *et al.* (1996), Lee and Saio (1997), and Townsend (2003a) discussed in great detail the $\lambda(s)$ dependence and asymptotic properties of the Hough functions. Here, we recall only the essentials.

For specified m and $s \rightarrow 0$, there are branches with $\lambda \rightarrow \ell(\ell + 1)$ and $\Theta(\theta) \rightarrow P_\ell^{|m|}$ (except for normalization). These branches correspond to g-modes distorted by rotation. For prograde sectorial modes ($m = \ell$), λ slowly decreases with s . For all other g-modes, the function $\lambda(s)$ is increasing quite rapidly. We will identify g-mode branches by the ℓ value at $s = 0$. Thus, like in the case of no rotation, we will use (ℓ, m) values as the angular quantum numbers and refer to ℓ as the mode degree. However, now specification of the angular dependence requires also the value of s . The symmetry about the equatorial plane is determined by the parity of $\ell + |m|$. If it is even, the functions $\Theta(\theta)$ and $\tilde{\Theta}(\theta)$ are symmetrical and $\hat{\Theta}(\theta)$ is antisymmetrical. The opposite is true if $\ell + |m|$ is odd. The branches for which $\lambda \rightarrow -\infty$ at $s \rightarrow 0$ correspond to r-modes. For each $m < 0$, there is one branch crossing zero at $s = |m| + 1$. If $\lambda > 0$, the associated modes become propagatory in the radiative regions, they may be excited and visible in the light variations. However, following Lee (2006), we will still call them *r*-modes. The functions $\Theta(\theta)$ and $\tilde{\Theta}(\theta)$ are antisymmetrical and $\hat{\Theta}(\theta)$ is symmetrical about the equator for these r-modes.

Upon replacing $\ell(\ell + 1)$ with $\lambda(s)$, the nonadiabatic mode properties may be calculated with a reasonable accuracy using the same code as for non-rotating stars. This is so because for the mode of our interest, horizontal flux losses, which are not correctly described, are small. The latitudinal dependence of perturbed thermodynamical parameters is then given by $\Theta(\theta)$. Thus, the bolometric flux perturbation may be written as

$$\frac{\delta\mathcal{F}_{\text{bol}}}{\mathcal{F}_{\text{bol}}} = \varepsilon f \Theta Z, \quad (4)$$

where f is a complex quantity determined by solution of linear nonadiabatic equations and it depends on the stellar model and the mode parameters m , λ and ω .

For evaluation of perturbed monochromatic fluxes, we also need the perturbed gravity, which, as follows from Eq. (1), is given by

$$\frac{\delta g}{g} = -\varepsilon(2 + \varpi^{-1})\Theta Z. \quad (5)$$

The effect of gravity perturbation plays a relatively small role in light variability caused by slow modes but it is easy to include. More important is perturbation of star shape leading to changes in the projected surface element and the limb-darkening. For both we need the normal to stellar surface which, as follows from Eq. (1), is given by

$$\delta\mathbf{n}_s = -\varepsilon\nabla_H(\Theta Z) = -\varepsilon\left(0, \frac{\partial\Theta}{\partial\theta}, \frac{im\Theta}{\sin\theta}\right)Z. \quad (6)$$

The change of the directed element of the surface is

$$\frac{\delta d\mathbf{S}}{dS} = \varepsilon \left(2\Theta, -\frac{\partial\Theta}{\partial\theta}, -\frac{im\Theta}{\sin\theta} \right) \mathbf{Z} \quad (7)$$

where $dS = R^2 d\mu d\varphi$.

From Eq. (1), we also obtain the perturbed pulsation velocity field as seen from an inertial system ($\varphi_0 = \varphi + \Omega t$)

$$\delta\mathbf{v} = \frac{d\xi}{dt} = \left(\frac{\partial}{\partial t} + \Omega \frac{\partial}{\partial\varphi_0} \right) \xi = \varepsilon R [-i\omega\xi + \Omega\mathbf{e}_z \times \xi]. \quad (8)$$

Use of the Lagrangian pulsational velocity is adequate for representing velocity at the photospheric layer because ξ is nearly constant across the outer layers for the slow modes considered by us.

3 Light Variation

3.1 Semi-Analytical Formula

The most straightforward extension of the expression for the light variation to the case of rotating stars is through the expansion of the Hough function into the truncated series of the associated Legendre functions. This was the way Townsend (2003b) derived his expression. We write the equivalent expression in the form, which is a straightforward generalization of our formula (Daszyńska-Daszkiewicz, Dziembowski and Pamyatnykh 2003) derived for the case of modes described by single spherical harmonic. Now the complex amplitude of the light variation in the x passband may be expressed as

$$\mathcal{A}_x(i) = \varepsilon \sum_{j=1}^{\infty} \gamma_{\ell_j}^m(s) Y_{\ell_j}^m(i, 0) \left[\mathcal{D}_{\ell_j}^x f + \mathcal{E}_{\ell_j}^x \right] \quad (9)$$

where

$$\ell_j = \begin{cases} |m| + 2(j-1) & \text{even - parity modes} \\ |m| + 2(j-1) + 1 & \text{odd - parity modes} \end{cases}$$

and

$$\begin{aligned} \mathcal{D}_{\ell}^x &= -1.086 b_{\ell}^x \frac{1}{4} \frac{\partial \log(\mathcal{F}_x |b_{\ell}^x|)}{\partial \log T_{\text{eff}}}, \\ \mathcal{E}_{\ell}^x &= -1.086 b_{\ell}^x \left[(2 + \ell)(1 - \ell) - (2 + \varpi^{-1}) \frac{\partial \log(\mathcal{F}_x |b_{\ell}^x|)}{\partial \log g} \right], \\ b_{\ell}^x &= \int_0^1 h_x(\tilde{\mu}) \tilde{\mu} P_{\ell}(\tilde{\mu}) d\tilde{\mu}. \end{aligned} \quad (10)$$

where h_x is the limb-darkening law, adopted in the nonlinear form (Claret 2000). With this form Townsend obtained his analytical expressions for b_{ℓ}^x . The quantities $\gamma_{\ell_j}^m(s)$, which have to be calculated numerically, are the expansion coefficients of the Θ function into the series of the Legendre functions. That is

$$\Theta(\theta) = \sum_{j=1}^{\infty} \gamma_{\ell_j}^m(s) P_{\ell_j}^m(\theta). \quad (11)$$

The expression given by Eq. (9) is quite revealing. At specified ε , the light amplitudes of low degree modes must decrease with s because of increasing role of higher

order terms which suffer more from disk-averaging. The higher order terms lead to the aspect-dependence of the amplitude ratios.

Unfortunately, we could not find a corresponding semi-analytical expression for the radial velocity and this is why we decided to rely on two-dimensional numerical integration over the visible hemisphere. We used Eq. (9) to check the accuracy.

3.2 Numerical Approach

The total flux in the x passband toward the observer is given by

$$L_x = \int_S \mathcal{F}_x h_x \mathbf{n}_{\text{obs}} \cdot d\mathbf{S} \quad (12)$$

where integration is carried over visible part of star surface, S , and \mathbf{n}_{obs} is the unit vector toward observer.

In the spherical coordinate system with the polar axis parallel to the rotation axis, we have

$$\mathbf{n}_{\text{obs}} \equiv (o_r, o_\theta, o_\varphi) \quad (13)$$

where

$$\begin{aligned} o_r &\equiv \tilde{\mu} = \cos i \cos \theta + \sin i \sin \theta \cos(\varphi - \varphi_0), \\ o_\theta &= -\cos i \sin \theta + \sin i \cos \theta \cos(\varphi - \varphi_0), \\ o_\varphi &= -\sin i \sin(\varphi - \varphi_0). \end{aligned}$$

The observer's angular coordinates are (i, φ_0) . The first order perturbation of the total flux is given by

$$\delta L_x = \int_S [(\delta \mathcal{F}_x h_x + \mathcal{F}_x \delta h_x) d\mathbf{S} \mathbf{e}_r + \mathcal{F}_x h_x \delta d\mathbf{S}] \cdot \mathbf{n}_{\text{obs}}. \quad (14)$$

Assuming an equilibrium atmosphere, we have from Eqs. (4) and (5)

$$\delta \mathcal{F}_x = \varepsilon \left[\frac{\alpha_T^x}{4} f - \alpha_g^x (2 + \varpi^{-1}) \right] \Theta Z$$

where

$$\alpha_T^x = \frac{\partial \log \mathcal{F}_x}{\partial \log T_{\text{eff}}} \quad \text{and} \quad \alpha_g^x = \frac{\partial \log \mathcal{F}_x}{\partial \log g}$$

are the derivatives determined numerically from grids of stellar atmosphere models. For perturbed limb darkening, we take into account perturbations of the coefficients on T_{eff} and g though they are only secondary contributors to light variation. More important contribution arises from $\delta \mathbf{n}_s$ (see Eq. 6). With all terms included, we obtain

$$\delta h_x = \varepsilon \left\{ \left[\frac{\partial h_x}{\partial \ln T} \frac{f}{4} - \frac{\partial h_x}{\partial \ln g} (2 + \varpi^{-1}) \right] - \frac{\partial h_x}{\partial \tilde{\mu}} \left(\frac{\partial \Theta}{\partial \theta} o_\theta + \frac{\text{im} \Theta}{\sin \theta} o_\varphi \right) \right\} \Theta Z.$$

The derivatives of Claret's h_x are given in Appendix A1. The expression for perturbed surface element is given in Eq. (7). The integration is carried over the unperturbed visible hemisphere. Within the linear approximation, the integration boundary is unchanged. Note also that the horizontal component of the displacement does not enter the expression. The domains of integration over θ and φ are shown in Fig. 1 and Fig. 2, respectively. From Figs. 1 and 2 it follows that the ranges are:

$$0 \leq \theta \leq \frac{\pi}{2} + i,$$

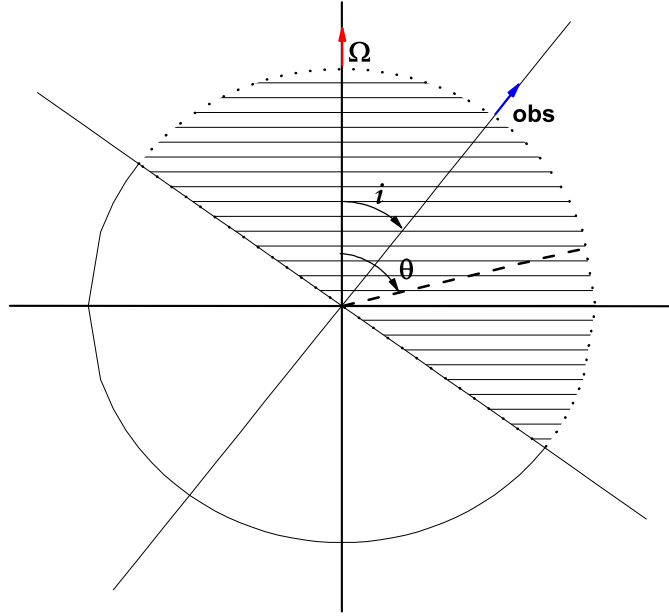


Fig. 1. The meridional view of the integration area.

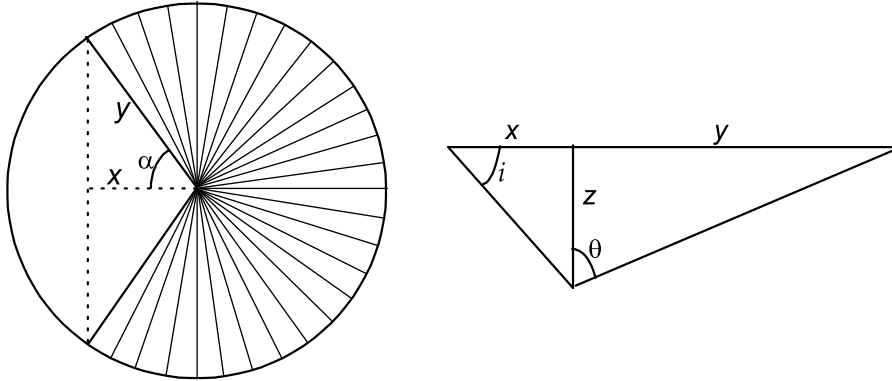


Fig. 2. Integration area over the azimuthal angle (left) and the edge-on view (right).

$$-(\pi - \alpha) \leq \varphi - \varphi_0 \leq (\pi - \alpha)$$

where $\alpha = \arccos[\cot\theta \cot i]$. For each θ , we carry the integration over the azimuthal angle, $\Psi = \varphi - \varphi_0$, from $-\beta$ to $+\beta$, where $\beta = \pi - \alpha = \pi - \arccos[\cot\theta \cot i]$ (see Fig. 1 and Fig. 2). We use identities

$$\int_{-\beta}^{\beta} G(\Psi) Z d\Psi = \begin{cases} 2 \int_0^{\beta} G(\Psi) \cos m\Psi d\Psi & \text{if } G(\Psi) \text{ is even} \\ 2i \int_0^{\beta} G(\Psi) \sin m\Psi d\Psi & \text{if } G(\Psi) \text{ is odd} \end{cases}$$

The final expression for the total light variation can be written in the following form

$$\frac{\delta L_x}{L_x} = \varepsilon \left[\left(\frac{\alpha_T^x}{4} \mathcal{B}_1 + \mathcal{B}_3 \right) f + 2\mathcal{B}_1 + \mathcal{B}_2 - (2 + \varpi^{-1})(\alpha_g^x \mathcal{B}_1 + \mathcal{B}_4) \right] Z_0 \quad (15)$$

and $Z_0 = \exp[i(m\varphi_0 - \omega t)]$. In Appendix A2 we give explicit expressions for the two-dimensional integrals, \mathcal{B} , which depend on two angular numbers, spin and the aspect.

The integrals take into account changes in the limb-darkening resulting from the change of the normal (Eq. 6) as well as the change due to perturbation of the local temperature (Eq. 4) and gravity (Eq. 5). The two latter are given through derivatives of h_x with respect to $\log T_{\text{eff}}$ and $\log g$. There are many terms contributing to δL_x . However, in our applications two are far dominant: the one resulting from temperature perturbation, which is proportional to $\alpha_T^x \mathcal{B}_1$, and the other resulting from the surface distortion, which is proportional to \mathcal{B}_2 .

4 Radial Velocity Variation

Adopting the standard sign convention, we write the radial velocity averaged over the stellar disk in the following form:

$$\langle V_{\text{rad}} \rangle = -\frac{\int_{S_0} (\mathbf{v} \cdot \mathbf{n}_{\text{obs}}) \mathcal{F} h_x \mathbf{n}_{\text{obs}} \cdot d\mathbf{S}}{\int_{S_0} \mathcal{F} h_x \mathbf{n}_{\text{obs}} \cdot d\mathbf{S}} \quad (16)$$

where for the total velocity field we use

$$\mathbf{v} = \delta\mathbf{v} + \Omega R \sin\theta \mathbf{e}_\varphi. \quad (17)$$

The pulsational component, $\delta\mathbf{v}$, as results from Eqs. (1) and (8), is given by

$$\delta\mathbf{v} = -i\omega\epsilon R \begin{pmatrix} \Theta - \frac{s}{2}\varpi\tilde{\Theta} \\ \varpi \left[\frac{\hat{\Theta}}{\sin\theta} - \frac{s \cos\theta}{2 \sin\theta} \tilde{\Theta} \right] \\ -i\varpi \left[\frac{\tilde{\Theta}}{\sin\theta} - \frac{s \cos\theta}{2 \sin\theta} \hat{\Theta} \right] + i\frac{s}{2}\Theta \sin\theta \end{pmatrix} \mathbf{Z} \quad (18)$$

The contribution of rotation to the mean radial velocity arises from the same pulsational changes of photospheric parameters which cause luminosity change and may be calculated in the same way as outlined in Section 3. Clearly, there is a nonzero contribution only for non-axisymmetric modes.

We write our final expression for the perturbed radial velocity in the following form,

$$\delta\langle V_{\text{rad}} \rangle = i\omega\epsilon R (C_{\text{puls}} + C_{\text{rot}}) Z_0, \quad (19)$$

with

$$C_{\text{puls}} = \left(\mathcal{B}_5 - \frac{s}{2} \mathcal{B}_7 \right) + \varpi \left(\mathcal{B}_6 - \frac{s}{2} \mathcal{B}_8 \right)$$

and

$$C_{\text{rot}} = -\frac{s \sin i}{2} \left[\left(\frac{1}{4} \alpha_T^x \mathcal{B}_9 + \mathcal{B}_{11} \right) f + 2\mathcal{B}_9 + \mathcal{B}_{10} - (2 + \varpi^{-1}) (\alpha_g^x \mathcal{B}_9 + \mathcal{B}_{12}) \right].$$

Explicit expressions for the \mathcal{B} coefficients in terms of the three Hough functions are given in Appendix A3.

If $s \approx 1$ and $m \neq 0$, the two contributions are of the same order. Similarly to the case of the luminosity, the dominant contributions to C_{rot} are the ones resulting from temperature perturbation, which here is proportional to $\alpha_T^x \mathcal{B}_9$, and the other resulting from the surface distortion, which is proportional to \mathcal{B}_{10} .

5 Unstable Modes in a $6 M_{\odot}$ Main Sequence Star

To illustrate how visibility of various modes depends on equatorial velocity of rotation we choose a model of a $6 M_{\odot}$ Population I star in the mid of its main sequence evolution. Parameters of the model are given in Table 1. The model is spherically symmetric, which is consistent with our use of the traditional approximation, but includes averaged effects of centrifugal force corresponding to uniform rotation with equatorial velocity of 250 km/s. The mean effects of centrifugal force are still reasonably small and therefore we used the same model to study effects of the Coriolis force at lower equatorial velocities.

There are many low frequency modes that are unstable in our selected star model. These are mainly g-modes. However, at sufficiently high rotation rate there are also certain r-modes, which become propagatory in radiative envelope and may become unstable. In all cases, the instability is caused by the κ -mechanism acting in the metal opacity bump layer. For g-modes, the angular order, ℓ , is defined at the limit of zero rotation where the angular dependence of amplitude is described by individual spherical harmonics. The actual mode geometry is determined by the (ℓ, m) numbers and the spin parameter, s . Since at each azimuthal order $m < 0$ there is only one r-mode for which λ changes sign, we will identify r-modes by the m value alone. Naturally, we focus attention on modes suffering least reduction of observable amplitude caused by disk-averaging. Therefore, we consider g-modes with $\ell \leq 2$ and r-modes with $m = -1$ and -2 .

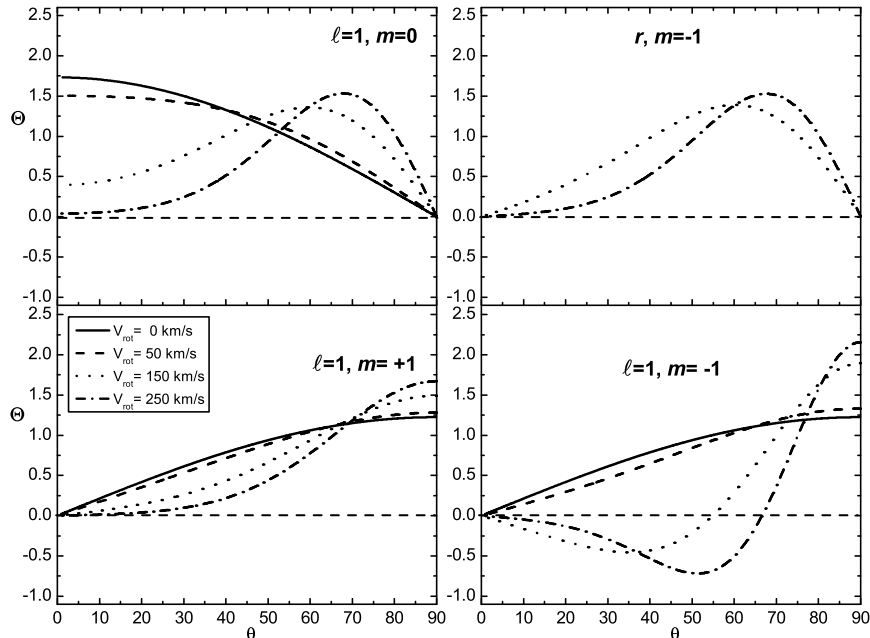


Fig. 3. The Hough functions for the selected g-modes with $\ell = 1$ and r-modes with $m = -1$ (see Table 1 for more data on the modes).

Typically, at each degree and azimuthal order, we find instability extending over many (up to 40) radial orders. For analysis of visibility, we selected the mode characterized by the highest normalized growth rate, η , which varies between -1 and 1 . The important parameters of the selected modes at adopted equatorial velocities are listed in Table 1. For the r-modes we write \dot{z} instead of ℓ as the first entry. The effect of rotation on mode surface geometry at specified V_{rot} depends on s which determines λ .

Table 1

Most unstable low degree modes in the B star model with $M = 6.0 M_{\odot}$, $\log T_{\text{eff}} = 4.205$, $\log L/L_{\odot} = 3.204$, for the four values of rotational velocity

ℓ	m	V_{rot}	spin	λ	ϖ	f	v_{obs} [c/d]	v_{star} [c/d]	η
1	0	0	0.00	2.00	17.76	(9.99, 11.55)	0.4220	0.4220	0.110
1	0	50	0.86	2.33	16.35	(10.56, 12.18)	0.4396	0.4396	0.129
1	0	150	1.97	4.62	9.48	(8.55, 13.02)	0.5772	0.5772	0.202
1	0	250	2.65	7.61	6.16	(5.82, 12.46)	0.7162	0.7162	0.238
1	+1	0	0.00	2.00	17.76	(9.99, 11.55)	0.4220	0.4220	0.110
1	+1	50	1.02	1.45	22.70	(10.38, 10.87)	0.5627	0.3731	0.063
1	+1	150	3.27	1.17	26.11	(10.00, 10.19)	0.9167	0.3478	0.031
1	+1	250	5.63	1.09	27.82	(10.33, 10.14)	1.2851	0.3369	0.021
1	-1	0	0.00	2.00	17.76	(9.99, 11.55)	0.4220	0.4220	0.110
1	-1	50	0.72	3.60	11.37	(8.98, 12.61)	0.3375	0.5271	0.179
1	-1	150	1.32	11.80	4.25	(3.42, 11.27)	0.2930	0.8619	0.258
1	-1	250	1.71	22.21	2.57	(0.42, 8.50)	0.0870	1.1097	0.265
2	0	0	0.00	6.00	7.35	(6.46, 12.38)	0.6569	0.6569	0.225
2	0	50	0.54	6.84	6.42	(5.41, 11.92)	0.7015	0.7015	0.234
2	0	150	1.24	13.37	3.76	(2.43, 10.46)	0.9170	0.9170	0.261
2	0	250	1.66	23.56	2.42	(0.02, 7.93)	1.1421	1.1421	0.265
2	+1	0	0.00	6.00	7.35	(6.46, 12.38)	0.6569	0.6569	0.225
2	+1	50	0.58	6.02	7.28	(6.41, 12.36)	0.8484	0.6587	0.225
2	+1	150	1.52	8.29	5.66	(5.11, 12.09)	1.3162	0.7473	0.244
2	+1	250	2.21	11.69	4.29	(3.50, 11.33)	1.8062	0.8580	0.257
2	-1	0	0.00	6.00	7.35	(6.46, 12.38)	0.6569	0.6569	0.225
2	-1	50	0.52	7.46	5.89	(4.74, 11.58)	0.5426	0.7322	0.239
2	-1	150	1.07	19.16	2.80	(0.68, 8.75)	0.4937	1.0626	0.265
2	-1	250	1.37	38.86	1.66	(-1.79, 4.43)	0.4315	1.3797	0.254
2	+2	0	0.00	6.00	7.35	(6.46, 12.38)	0.6569	0.6569	0.225
2	+2	50	0.60	5.18	7.91	(6.23, 11.88)	1.0110	0.6317	0.213
2	+2	150	1.93	4.52	9.05	(7.24, 12.22)	1.7286	0.5908	0.202
2	+2	250	3.29	4.31	9.49	(7.60, 12.32)	2.4733	0.5770	0.198
2	-2	0	0.00	6.00	7.35	(6.46, 12.38)	0.6569	0.6569	0.225
2	-2	50	0.51	7.57	5.81	(4.63, 11.51)	0.3583	0.7375	0.239
2	-2	150	1.21	14.01	3.59	(2.08, 10.13)	0.1992	0.9384	0.262
2	-2	250	1.66	23.52	2.43	(0.04, 7.95)	0.7552	1.1411	0.265
r	-1	150	2.61	2.45	16.67	(11.81, 12.77)	0.1336	0.4352	0.131
r	-1	250	3.20	4.87	9.00	(8.12, 12.92)	0.3557	0.5924	0.208
r	-2	150	3.39	1.36	28.11	(14.05, 11.73)	0.8025	0.3352	0.040
r	-2	250	3.90	3.27	13.37	(11.31, 13.39)	1.4103	0.4859	0.164

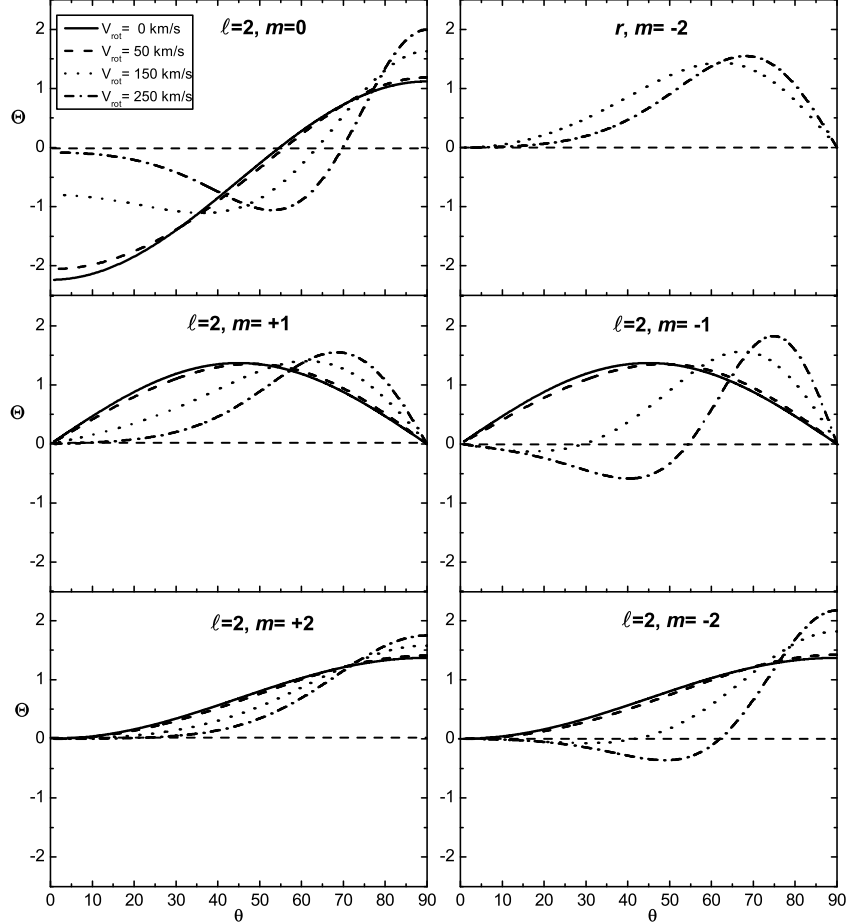


Fig. 4. Same as Fig. 3 but for the g-modes with $\ell = 2$ and r-modes with $m = -2$.

The depth-dependence of eigenfunctions is determined primarily by the product $\lambda\bar{\omega}$. In particular, the radial orders in this model are given by $n \approx 4.23\sqrt{\lambda\bar{\omega}}$. For the selected modes they are between 26 and 34. Nonadiabatic parameters, f and η , depend on n but also on the pulsation frequency in the star reference system, v_{star} .

The Hough Θ -functions for selected modes are shown in Figs. 3 and 4. We may see the well-known effect of equatorial amplitude confinement, which increases with V_{rot} . The effect is present in all modes including those with $m = \ell$ though $\lambda(s)$ is a decreasing function in these cases. As for the remaining Hough functions, which are important, the confinement is also present. $\hat{\Theta}$ and Θ have the same symmetry about the equator and the symmetry of $\hat{\Theta}$ is opposite.

6 Visibility of Slow Modes

For the modes listed in Table 1, we calculated amplitudes of light variation in the U and V Geneva passbands, A_U and A_V , with Eqs. (15), as well as that of the radial velocity, $A_{V_{\text{rad}}}$, with Eqs. (19), adopting an arbitrary normalization, $\varepsilon = 0.01$. Coefficients α_T and α_g occurring in Eq. (15), were interpolated from the line-blanketed models of stellar atmospheres (Castelli and Kurucz 2004).

Figs. 5–7 show the A_V and $A_{V\text{rad}}$ in function of the aspect angle. Because of the arbitrary normalization, they cannot be regarded as reliable predictors of expected amplitudes. We may expect that chances of excitation are related to η but it does not determine ε . Still plots like these provide important hints for interpretation of the rich oscillation spectra such as that of HD 163868 (Walker *et al.* 2005b). For the $\ell = 1$ g-modes we see a simple patterns in the dependence of A_V on the rotation rate. The aspect-dependence is qualitatively the same as in the case of no rotation. Rotation gives rise to a departure from the dipolar angular dependence of ξ_r and $\delta\mathcal{F}_{\text{bol}}$ but the contribution of the surface distortion to light variation remains small even at $V_{\text{rot}} = 250$ km/s. Thus, the $A_V(i)$ -dependence is a simple reflection of the $\Theta(\theta)$ -dependence shown in Fig. 3. The equatorial confinement leads to a reduction of amplitude upon averaging contributions from the whole hemisphere.

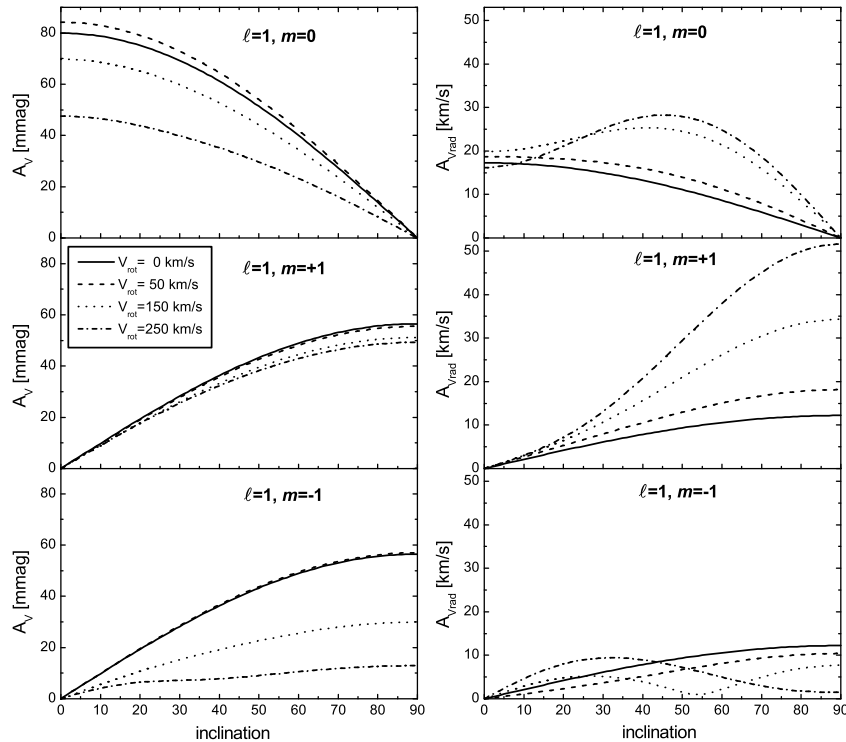


Fig. 5. Amplitudes of light in the V-band of Geneva photometry, A_V , and of the radial velocity, $A_{V\text{rad}}$, at indicated equatorial rotational velocities plotted as functions of the aspect angle, for the $\ell = 1$ g-modes. The amplitudes are calculated assuming $\varepsilon = 0.01$ (see Eq. 1).

The pattern of the dependence of radial velocity amplitude on the rotation rate, shown in the right panels of Fig. 5, is more complicated. In all three cases, the dominant contribution arises from pulsational velocity (the C_{puls} term in Eq. 19). A secondary but significant contribution, the C_{rot} term, adds in the case of prograde modes and subtracts in the case of retrograde modes. However, the main reason for the large difference between the modes and for the nonmonotonic aspect dependence is connected with properties of C_{puls} . At high rotation rates the contribution from the advective term in δv is large and causes that all its three components play a role. The large values of $A_{V\text{rad}}$ in the case of $\ell = 1, m = +1$ mode for the near equatorial observers arise primarily from this term. We see that at least for some aspects, fast rotation increases the chances for mode detection by means of radial velocity measurements. The $A_V(i)$ -dependencies for the $\ell = 2$ g-modes depicted in the left panels of Fig. 6, show that, despite of the increasing

equatorial confinement, the aspect of the best visibility moves toward the pole with increasing rotation rate. This somewhat unexpected feature, which has been already noted by Townsend (2003b), is explained in part by the effect of the surface distortion. There are aspects at which we see amplitude increase with V_{rot} but on average the effect is the same as for $\ell = 1$, that is fast rotation decreases chances for photometric detection of slow modes. Also on average, amplitudes of the $\ell = 2$ modes are lower than those of $\ell = 1$. In the right panels of Fig. 6, we may see that radial velocity amplitudes of prograde modes increase with the rotation rate and that the effect is opposite for the retrograde modes. The role of the C_{rot} term is much more significant than at $\ell = 1$.

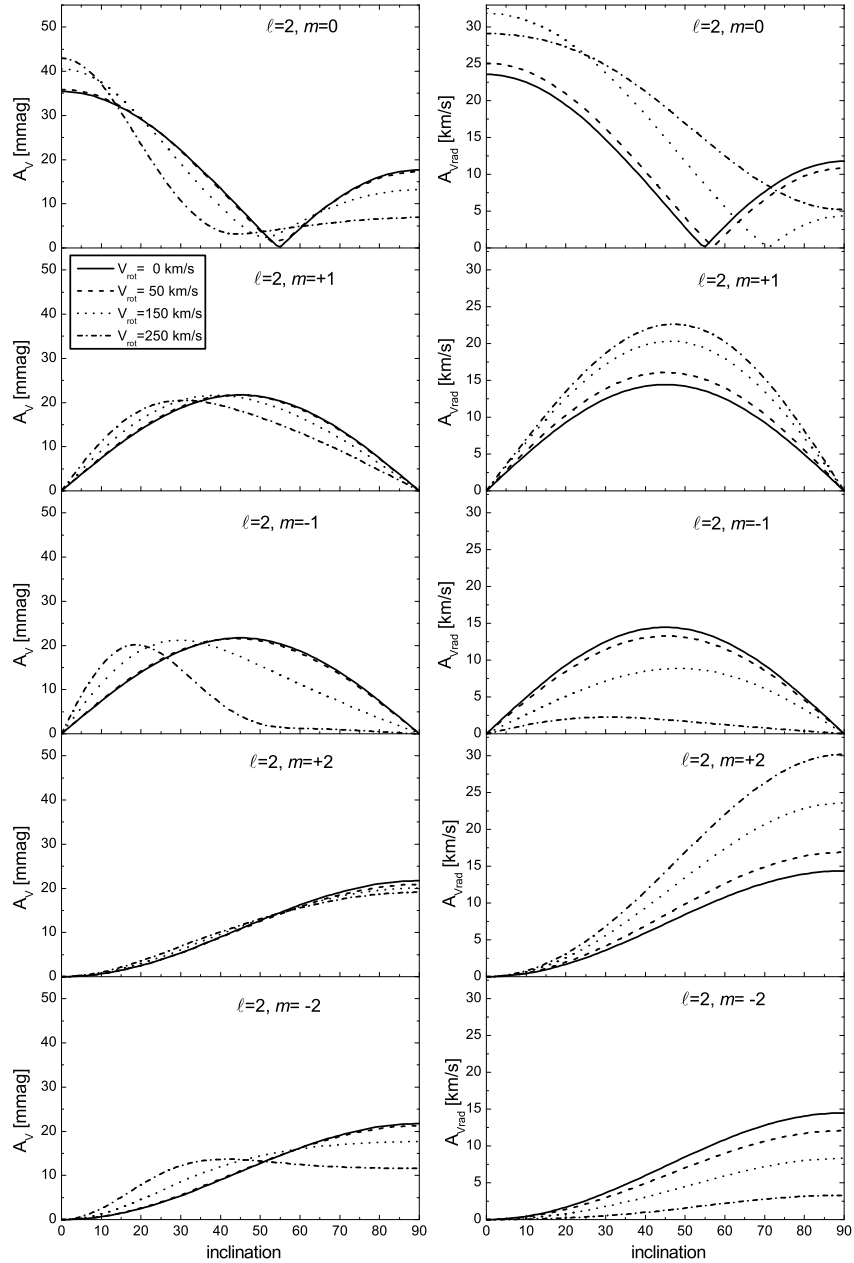


Fig. 6. Same as Fig. 5 but for the $\ell = 2$ g-modes.

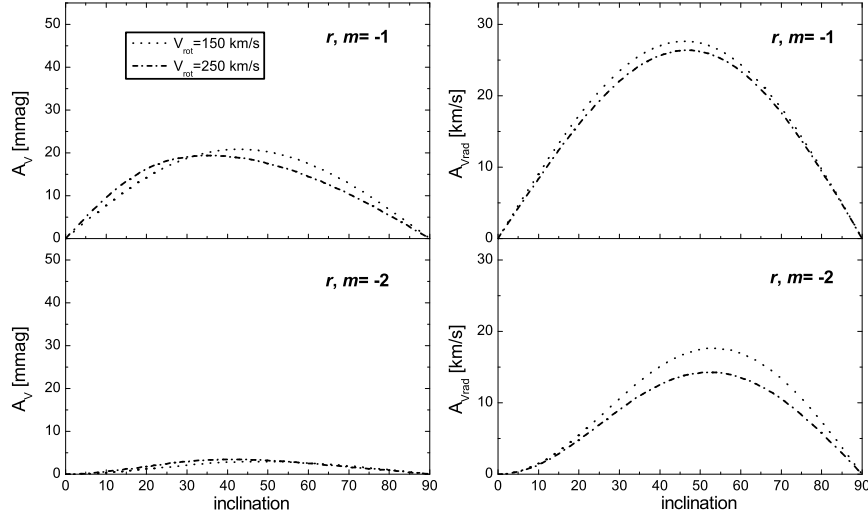


Fig. 7. Same as Fig. 5 but for the r-modes with $|m| \leq 2$.

We may see in Fig. 3 that $\Theta(\theta)$ for the $m = -1$ r-mode and for the $\ell = 1, m = 0$ g-mode look very similar. Likewise, in Fig. 4 we see the similarity of Θ 's for the $m = -2$ r-mode and for the $\ell = 2, m = +1$ g-mode. Yet, as we may see in Fig. 7, the photometric amplitudes of the r-modes are much smaller and have different aspect dependence. The amplitude reduction is in part caused by cancellations in the integral over ϕ . Moreover, the effect of distortion, which is significant, cancels a part of the effect of temperature perturbation. The r-modes are antisymmetric with respect to the equator and are best seen from the intermediate aspect angles. The radial velocity amplitudes, shown in the right panels of Fig. 7, are much less reduced. Thus, spectroscopy gives a better chance for detecting r-modes.

7 Prospects for Mode Discrimination

Rotation has a very profound effect on slow mode visibility and hence on the procedure of mode identification. Unlike in non-rotating stars, the amplitude ratios depend on the azimuthal order, m , and on the aspect, i . Modes with various m differ not only in the surface geometry but also in their nonadiabatic properties. There are constraints on m following from localization in the frequency spectrum. Modes differing in the sign of m are well separated. As we have seen in Figs. 5–7, the aspect is an important factor in mode selection which has to be taken into account considering possible m and i values. Nonetheless, a unique discrimination of modes is not likely possible without employing amplitude and phase data.

Let us begin with photometric data alone. The observables, which do not depend on ε , are amplitude ratios and phase differences from multiband photometry. In this case, the potential for mode discrimination rests mainly on the difference in the relative temperature and distortion contribution to the total light variation in different passbands. The latter contribution for the $\ell = 1$ g-modes is small, hence a discrimination between such modes might be difficult. However, as the plots in Fig. 8 show, these modes may be rather easily distinguished from the $\ell = 2$ and r-modes even if information about i and V_{rot} is imprecise. A discrimination between the two $\ell = 2$ modes could be difficult if the measured phase difference is between 0.2 and 0.3. The range is consistent with $m = -1$, if V_{rot} is between 150 km/s and 175 km/s, and $m = -2$, if V_{rot} is 250 km/s.

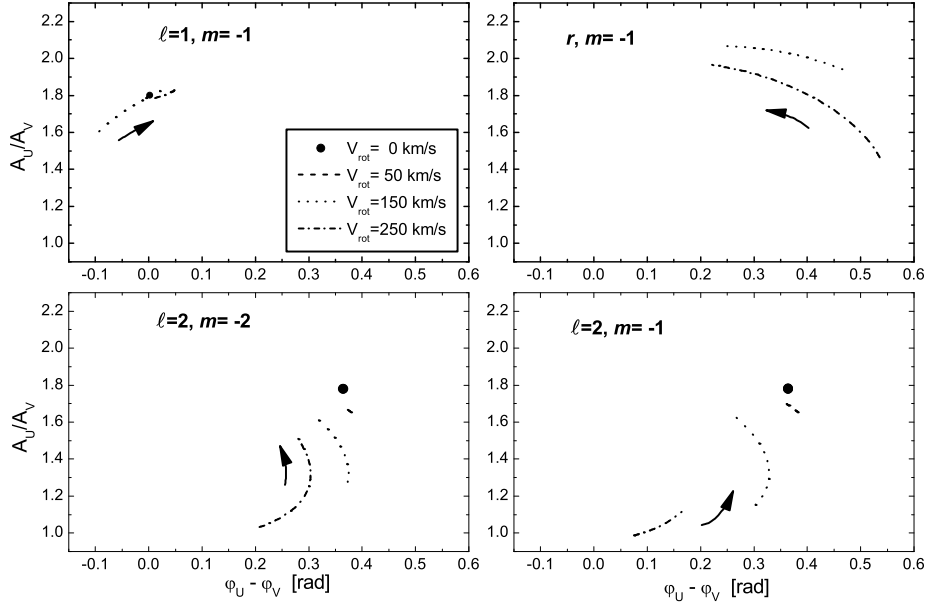


Fig. 8. Photometric diagnostic diagrams for selected modes based on light amplitudes and phases in the U and V Geneva passbands, for retrograde g-modes and for the r-mode with $m = -1$. The arrows indicate direction of increasing i . The i -ranges are limited by the condition $A_V > 10$ mmag

Any discrimination between these four modes based on frequencies alone would not be possible because all of them are retrograde and occupy the low frequency end of the oscillation spectrum. It is important to remember that the plots refer only to most unstable modes of each type. Thus, in real life, there is additional uncertainties in frequencies and in the f -values that affect the amplitude ratios and phase differences. With mean radial velocity data, discrimination between the two $\ell = 2$ modes should be unambiguous, as the plots in the lower panels of Fig. 9 show. In the upper panels we see that also distinguishing the two $\ell = 1$ modes should be easy. Disentangling the $m = +1$ and $m = 0$ cases, however, may require data on line profile changes.

The main benefit from radial velocity data is the possibility of simultaneous determination of ℓ with no need for specifying the value of the complex parameter f . Instead, as described in the case of non-rotating stars by Daszyńska-Daszkiewicz *et al.* (2005), the combined spectroscopy and photometry data on amplitudes and phases may be used to determine f , which becomes an independent seismic observable, and the mode degree, ℓ . In order to see how the method may be extended to the present case, let us rewrite Eqs. (15) and (19) as expressions for the complex amplitudes of light in the x -band and of radial velocity, respectively. From Eq. (15) we obtain

$$\mathcal{A}_x(i) = \mathcal{D}^x(i) f \tilde{\epsilon} + \mathcal{E}^x(i) \tilde{\epsilon} \quad (20)$$

where

$$\mathcal{D}^x(i) = -1.086 \left(\frac{\alpha_T^x}{4} \mathcal{B}_1 + \mathcal{B}_3 \right),$$

$$\mathcal{E}^x(i) = -1.086 [2\mathcal{B}_1 + \mathcal{B}_2 - (2 + \varpi^{-1})(\alpha_g^x \mathcal{B}_1 + \mathcal{B}_4)]$$

and $\tilde{\epsilon} = \epsilon \exp(im\phi_0)$. Similarly, from Eq. (19) the first moment of spectral line is equal to

$$\mathcal{M}_1^x(i) = i\omega R [\mathcal{H}^x(i) f \tilde{\epsilon} + \mathcal{G}^x(i) \tilde{\epsilon}] \quad (21)$$

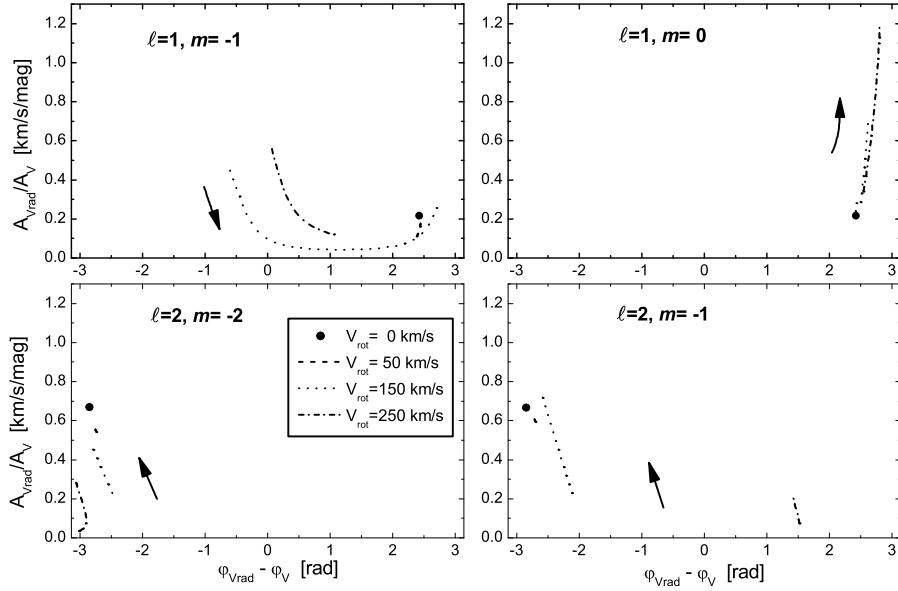


Fig. 9. Diagnostic diagrams for selected modes based on amplitudes and phases in the V Geneva photometric passband and in the radial velocity, for g -modes with $\ell = 1$ and 2.

where

$$\mathcal{H}^x(i) = -\frac{s \sin i}{2} \left(\frac{1}{4} \alpha_T^x \mathcal{B}_9 + \mathcal{B}_{11} \right)$$

and

$$\mathcal{G}^x(i) = \mathcal{B}_5 - \frac{s}{2} \mathcal{B}_7 + \varpi \left(\mathcal{B}_6 - \frac{s}{2} \mathcal{B}_8 \right) - \frac{s \sin i}{2} \left[2\mathcal{B}_9 + \mathcal{B}_{10} - (2 + \varpi^{-1}) (\alpha_g^x \mathcal{B}_9 + \mathcal{B}_{12}) \right].$$

These two equations are counterparts of Eqs. (1) and (2) of Daszyńska-Daszkiewicz *et al.* (2005).

In the case of negligible rotation, the dependence of amplitudes on m and i has been absorbed in $\tilde{\epsilon}$ and the problem was reduced to finding $\tilde{\epsilon}f$ and $\tilde{\epsilon}$ by the least square minimization of $\chi^2(\ell)$. The method requires stellar atmosphere parameters, which in fact may be improved on the process of pulsation amplitude fitting. A unique determination of ℓ is possible even with imprecise atmosphere parameters if the $\min(\chi^2)(\ell)$ dependence is strong. In the present case we have two more stellar parameters to improve which are i and V_{rot} . Moreover, we have to take into account the m -dependence. Prospects for mode identification depend on the strength of the $\min(\chi^2)(\ell, m)$ dependence. The plots in Figs. 8 and 9 suggest that it is likely the case. However, it remains to be seen when the method is applied to real data.

8 Summary and Conclusions

Our goal was to examine chances for detection and identification of slow oscillation modes whose frequencies are of the order of angular velocity of rotation. In our calculations of expected mode amplitudes, we relied on a nonadiabatic generalization of the traditional approximation, similar to that introduced by Townsend (2005a). The chances for detecting a particular mode depend, in part, on its intrinsic amplitudes, which may be calculated only in the framework of a nonlinear modeling. Our linear models give us only a hint which is the growth rate. Such models are expected to

be adequate for describing geometry of the mode which has important impact on mode visibility, its aspect and the angular degree dependence. With the formalism outlined in Sections 3 and 4, we calculated the observable amplitudes for selected unstable modes in models of a $6 M_{\odot}$ main sequence star as a function of the rotation rate and the aspect angle. The model may be regarded as representative for SPB variables.

Departure from the individual spherical-harmonic dependence which increases with the rotation rate leads, in most cases, to lower photometric amplitudes. In contrast, the effect on radial velocity amplitude is most often opposite. However, the light to radial velocity amplitude ratio changes significantly from mode to mode and depends on the aspect. We showed, in particular, that the mixed r/g-modes are most easily detectable in radial velocity. Considering possible identification of peaks in rich oscillation spectra such as of HD 163868 (Walker *et al.* 2005b) it is important to take into account the aspect dependence of considered mode amplitudes as it has been done by Dziembowski *et al.* (2007).

The observables yielding numerical constraints on mode geometry and the aspect angle are amplitude ratios and phase differences. We calculated examples of diagrams based on photometric data in two passbands and on mean radial velocity measurements. Not always photometric data are sufficient for mode discrimination. Radial velocity data not only help discrimination but also allow to proceed in a less model-dependent manner. The photospheric value of the complex radial eigenfunction corresponding to the radiative flux may then be determined from data rather than taken from linear nonadiabatic calculations. A comparison of calculated and deduced values yields a constraint on the model.

Acknowledgements. This work has been supported by the Polish MNiSW grant No 1 P03D 021 28.

REFERENCES

- Baade, D. 1982, *Astron. Astrophys.*, **10**, 65.
 Balona, L. 1995, *MNRAS*, **306**, 407.
 Bildsten, L., Ushomirsky, G., and Cutler, C. 1996, *Astrophys. J.*, **460**, 827.
 Castelli, F., and Kurucz, R.L. 2004, astro-ph/0405087 (<http://kurucz.harvard.edu>).
 Claret, A. 2000, *Astron. Astrophys.*, **363**, 1081.
 Daszyńska-Daszkiewicz, J., Dziembowski, W.A., and Pamyatnykh, A.A. 2003, *Astron. Astrophys.*, **407**, 999.
 Daszyńska-Daszkiewicz, J., Dziembowski, W.A., and Pamyatnykh, A.A. 2005, *Astron. Astrophys.*, **441**, 641.
 Dziembowski, W.A., Daszyńska-Daszkiewicz, J., and Pamyatnykh, A.A. 2007, *MNRAS*, **374**, 248.
 Jerzykiewicz, M., *et al.* 2005, *MNRAS*, **360**, 619.
 Lee, U. 2006, *MNRAS*, **365**, 677.
 Lee, U., and Saio, H. 1997, *Astrophys. J.*, **491**, 839.
 Savonije, G.J. 2005, *Astron. Astrophys.*, **443**, 557.
 Saio, H., *et al.* 2007, *Astrophys. J.*, **654**, 544.
 Townsend, R.H.D. 2003a, *MNRAS*, **340**, 1020.
 Townsend, R.H.D. 2003b, *MNRAS*, **343**, 125.
 Townsend, R.H.D. 2005a, *MNRAS*, **360**, 465.
 Townsend, R.H.D. 2005b, *MNRAS*, **364**, 573.
 Walker, G.A.H., *et al.* 2005a, *Astrophys. J. Letters*, **623**, L145.
 Walker, G.A.H., *et al.* 2005b, *Astrophys. J. Letters*, **635**, L77.

Appendix

A1. The Limb-Darkening Law

For calculating the surface integrals in Eq. (15) and Eq. (19), we need to specify the limb-darkening law. Here, we use the nonlinear Claret (2000) formulae which we rewrite in the following form

$$h_x(\tilde{\mu}) = 2 \frac{1 - \sum_{k=1}^4 a_k^x (1 - \tilde{\mu}^{k/2})}{1 - \sum_{k=1}^4 \frac{k}{k+4} a_k^x}.$$

The derivative with respect to $\tilde{\mu}$ can be easily obtained from this formula. The derivatives with respect to the effective temperature and gravity are given by:

$$\frac{\partial h_x}{\partial \ln T_{\text{eff}}} = \frac{1}{1 - \sum_{k=1}^4 \frac{k}{k+4} a_k^x} \cdot \sum_{k=1}^4 \left[\frac{k}{k+4} h_x - 2(1 - \tilde{\mu}^{k/2}) \right] \frac{\partial a_k^x}{\partial \ln T_{\text{eff}}},$$

and

$$\frac{\partial h_x}{\partial \ln g} = \frac{1}{1 - \sum_{k=1}^4 \frac{k}{k+4} a_k^x} \cdot \sum_{k=1}^4 \left[\frac{k}{k+4} h_x - 2(1 - \tilde{\mu}^{k/2}) \right] \frac{\partial a_k^x}{\partial \ln g}$$

respectively.

A2. Integrals in the Expression for the Light Variation

$$\mathcal{B}_1 = \int_0^{\frac{\pi}{2}+i} \Theta \mathcal{P}_1 \sin \theta \, d\theta$$

$$\mathcal{B}_2 = \int_0^{\frac{\pi}{2}+i} \left(\frac{\partial \Theta}{\partial \theta} \sin \theta \mathcal{P}_2 + m \Theta \mathcal{P}_3 \right) d\theta$$

$$\mathcal{B}_3 = \int_0^{\frac{\pi}{2}+i} \Theta \mathcal{P}_4 \sin \theta \, d\theta$$

$$\mathcal{B}_4 = \int_0^{\frac{\pi}{2}+i} \Theta \mathcal{P}_5 \sin \theta \, d\theta$$

where

$$\mathcal{P}_1 = \frac{1}{\pi} \int_0^{\beta} \cos m\Psi h_x o_r \, d\Psi$$

$$\mathcal{P}_2 = -\frac{1}{\pi} \int_0^{\beta} \cos m\Psi \left(o_r \frac{dh_x}{do_r} + h_x \right) o_\theta \, d\Psi$$

$$\mathcal{P}_3 = \frac{1}{\pi} \int_0^{\beta} \sin m\Psi \left(o_r \frac{dh_x}{do_r} + h_x \right) o_\phi \, d\Psi$$

$$\mathcal{P}_4 = \frac{1}{\pi} \int_0^\beta \cos m\Psi \frac{\partial h_x}{\partial \ln T_{\text{eff}}} o_r d\Psi$$

$$\mathcal{P}_5 = \frac{1}{\pi} \int_0^\beta \cos m\Psi \frac{\partial h_x}{\partial \ln g} o_r d\Psi.$$

The function Θ is one of three Hough functions (see Section 2). The components of the unit vector directed to the observer (o_r, o_θ, o_ϕ) are given in Eq. (13).

A3. Integrals in the Expression for the Radial Velocity Variation

$$\mathcal{B}_5 = \int_0^{\frac{\pi}{2}+i} \Theta \mathcal{P}_6 \sin \theta d\theta$$

$$\mathcal{B}_6 = \int_0^{\frac{\pi}{2}+i} (\hat{\Theta} \mathcal{P}_7 + \tilde{\Theta} \mathcal{P}_8) d\theta$$

$$\mathcal{B}_7 = \int_0^{\frac{\pi}{2}+i} \Theta \mathcal{P}_8 \sin^2 \theta d\theta$$

$$\mathcal{B}_8 = \int_0^{\frac{\pi}{2}+i} [\tilde{\Theta} \mathcal{P}_6 \sin \theta + (\tilde{\Theta} \mathcal{P}_7 + \hat{\Theta} \mathcal{P}_8) \cos \theta] d\theta$$

$$\mathcal{B}_9 = \int_0^{\frac{\pi}{2}+i} \Theta \mathcal{P}_9 \sin^2 \theta d\theta$$

$$\mathcal{B}_{10} = \int_0^{\frac{\pi}{2}+i} \left(\frac{\partial \Theta}{\partial \theta} \sin \theta \mathcal{P}_{10} + m \Theta \mathcal{P}_{11} \right) \sin \theta d\theta$$

$$\mathcal{B}_{11} = \int_0^{\frac{\pi}{2}+i} \Theta \mathcal{P}_{12} \sin^2 \theta d\theta$$

$$\mathcal{B}_{12} = \int_0^{\frac{\pi}{2}+i} \Theta \mathcal{P}_{13} \sin^2 \theta d\theta$$

where

$$\mathcal{P}_6 = \frac{1}{\pi} \int_0^\beta \cos m\Psi h_x o_r^2 d\Psi$$

$$\mathcal{P}_7 = \frac{1}{\pi} \int_0^\beta \cos m\Psi h_x o_r o_\theta d\Psi$$

$$\mathcal{P}_8 = \frac{1}{\pi} \int_0^\beta \sin m\Psi h_x o_r o_\phi d\Psi$$

$$\mathcal{P}_9 = \frac{1}{\pi} \int_0^\beta \sin m\Psi \sin \Psi h_x o_r d\Psi$$

$$\mathcal{P}_{10} = -\frac{1}{\pi} \int_0^\beta \sin m\Psi \sin \Psi \left(o_r \frac{dh_x}{do_r} + h_x \right) o_\theta d\Psi$$

$$\mathcal{P}_{11} = -\frac{1}{\pi} \int_0^\beta \cos m\Psi \sin \Psi \left(o_r \frac{dh_x}{do_r} + h_x \right) o_\varphi d\Psi$$

$$\mathcal{P}_{12} = \frac{1}{\pi} \int_0^\beta \sin m\Psi \sin \Psi \frac{\partial h_x}{\partial \ln T_{\text{eff}}} o_r d\Psi$$

$$\mathcal{P}_{13} = \frac{1}{\pi} \int_0^\beta \sin m\Psi \sin \Psi \frac{\partial h_x}{\partial \ln g} o_r d\Psi$$